

QCD phase diagram with isospin chemical potential*

Bastian B. Brandt and Gergely Endrődi

Institute for Theoretical Physics, Goethe University, Max-von-Laue-Strasse 1, 60438 Frankfurt am Main, Germany

E-mail: brandt@th.physik.uni-frankfurt.de,
endrodi@th.physik.uni-frankfurt.de

In this contribution we investigate the phase diagram of QCD in the presence of an isospin chemical potential. To alleviate the infrared problems of the theory associated with pion condensation, we introduce the pionic source as an infrared regulator. We discuss various methods to extrapolate the results to vanishing pionic source, including a novel method based on the singular value spectrum of the massive Dirac operator, a leading-order reweighting and a spline Monte-Carlo fit. Our main results concern the phase transition boundary between the normal and the pion condensation phases and the chiral/deconfinement transition temperature as a function of the chemical potential. In addition, we perform a quantitative comparison between our direct results and a Taylor-expansion obtained at zero chemical potential to assess the applicability range of the latter.

34th annual "International Symposium on Lattice Field Theory"

24-30 July 2016

University of Southampton, UK

*This contribution contains the combined proceedings of the two talks presented by the authors at the conference: 'QCD with isospin chemical potential: low densities and Taylor expansion' and 'QCD with isospin chemical potential: pion condensation'.

1. Introduction

Quantum Chromodynamics (QCD) is the theory of the strong interactions. It describes how protons and neutrons are built up of elementary particles: quarks and gluons. For various physical applications ranging from the evolution of the early universe through neutron star physics to heavy-ion collisions, it is of interest how quarks and gluons behave if the system is heated up or is compressed. The relevant parameters in this context are the temperature T and the quark densities n_f for each quark flavor f . For most of the above scenarios only the light quarks $f = u, d, s$ contribute. In the grand canonical ensemble, the densities are traded for the corresponding chemical potentials μ_f as conjugate parameters. Instead of working in the flavor basis, it is customary to introduce the three independent combinations

$$\mu_B = \frac{3}{2}(\mu_u + \mu_d), \quad \mu_I = \frac{1}{2}(\mu_u - \mu_d), \quad \mu_S = -\mu_s, \quad (1.1)$$

being the baryon, isospin, and strangeness chemical potentials. On timescales relevant for the strong interactions – where flavor-changing weak processes are ineffective – all three densities are conserved and working with the corresponding chemical potentials is justified.

While μ_B and μ_S couple to baryon number and strangeness, μ_I couples to the difference of the number of protons and neutrons. Thus, it is a relevant parameter for systems with an asymmetry between protons and neutrons. Two prime examples that exhibit such an asymmetry are the core of neutron stars and the initial state of heavy-ion collisions. Since neutrons dominate over protons in both cases, these systems are characterized by a negative isospin chemical potential $\mu_I < 0$. At the same time, the nonzero baryon number implies $\mu_B > 0$.

One of the most effective systematic approaches to study the physics of quarks and gluons is by means of numerical simulations of the QCD path integral on a Euclidean space-time lattice. These simulations employ standard importance sampling techniques, which rely on the probabilistic interpretation of $\exp(-S_{\text{QCD}})$, where S_{QCD} is the QCD action. However, for nonzero baryon or strangeness chemical potentials, S_{QCD} becomes complex. This is the so-called complex action problem (sign problem) that invalidates direct Monte-Carlo simulations. Fortunately, the sign problem does not affect nonzero isospin, since S_{QCD} remains real for $\mu_I \neq 0$.

In the present contribution we consider the impact of a nonzero isospin chemical potential on the phase structure of QCD, and set $\mu_B = \mu_S = 0$. Although not directly related to the above described physical situations, this system captures an interesting phenomenon that might be relevant for neutron stars and for nuclear physics – the condensation of pions [1, 2]. Indeed, it is known from chiral perturbation theory [3] that at the threshold value $\mu_I = m_\pi/2$, a second-order phase transition takes place and the ground state transforms to a Bose-Einstein condensate of pions.

Besides this phenomenological motivation, there are various conceptual and technical similarities between the theory at nonzero isospin and that at nonzero baryon density. In both cases the zero-temperature behavior of the theory involves the so-called Silver Blaze phenomenon [4] – where the chemical potential affects the fermionic action but has no impact on the ground state – followed by particle creation beyond a threshold chemical potential. In addition, beyond the threshold a proliferation of near-zero eigenvalues takes place, leading to an ill-conditioned fermion matrix and numerical problems for its inversion, i.e., for the simulation algorithm. This necessitates the use of an infrared regulator that we denote by λ below. Understanding these concepts and

facing these technical challenges in the (sign-problem-free) $\mu_I \neq 0$ theory may give us insight on how to assess the $\mu_B \neq 0$, $\mu_S \neq 0$ system in the future, once the sign problem has been circumvented.

Lattice QCD with nonzero μ_I has already attracted considerable amount of interest, see, e.g., Refs. [5 – 10]. In this contribution we improve our understanding of this system by simulating at the physical value of the pion mass and by using an improved staggered action. In addition, we develop a novel method for the extrapolation of the infrared regulator λ to zero. This method involves the singular values of the massive Dirac operator, which we discuss for the first time on the lattice in this context. The extrapolated results allow for a determination of the phase boundary between the normal and the pion condensed phase and of the chiral/deconfinement transition line in the phase diagram. Yet another use of our results is the possibility to directly check the applicability range of a Taylor-expansion in μ_I around $\mu_I = 0$. Our quantitative comparison gives a hint on how far similar expansions in the baryon chemical potentials might be reliable.

2. Simulation setup and observables

We consider three-flavor QCD with degenerate light quark masses $m_u = m_d \equiv m_{ud}$ and strange quark mass m_s at temperature T and in a finite volume V . The theory is discretized on a $N_s^3 \times N_t$ space-time lattice with spacing a using stout smeared rooted staggered quarks and tree-level Symanzik improved gluons. The quark masses are tuned to their physical values along the line of constant physics $m_f(\beta)$. This tuning, together with the simulation algorithm and the action at $\mu_I = 0$ is detailed in Ref. [11], while the implementation of the chemical potential follows Ref. [10]. The partition function of the system is given in terms of the path integral over the gluon links U ,

$$\mathcal{Z} = \int \mathcal{D}U e^{-\beta S_G} (\det \mathcal{M}_{ud})^{1/4} (\det \mathcal{M}_s)^{1/4}, \quad (2.1)$$

where $\beta = 6/g^2$ denotes the inverse gauge coupling, S_G is the gluon action, \mathcal{M}_{ud} is the light quark matrix in up-down basis and \mathcal{M}_s is the strange quark matrix,

$$\mathcal{M}_{ud} = \not{D}(\tau_3 \mu_I) + m_{ud} \mathbb{1} + i\lambda \eta_5 \tau_2 = \begin{pmatrix} \not{D}(\mu_I) + m_{ud} & \lambda \eta_5 \\ -\lambda \eta_5 & \not{D}(-\mu_I) + m_{ud} \end{pmatrix}, \quad \mathcal{M}_s = \not{D}(0) + m_s. \quad (2.2)$$

Here, \not{D} is the massless Dirac operator and τ_i denote the Pauli matrices. The off-diagonal term in \mathcal{M}_{ud} involves the pionic source λ , which was briefly mentioned in the introduction and whose role will be explained in more detail below. The matrix $\eta_5 = (-1)^{n_x+n_y+n_z+n_t}$ is positive (negative) on even (odd) sites and is the staggered equivalent of γ_5 . A direct Monte-Carlo simulation of this system is feasible because of positivity for $\lambda > 0$ and $m_s > 0$,

$$\det \mathcal{M}_{ud} = \det (|\not{D}(\mu_I) + m_{ud}|^2 + \lambda^2) > 0, \quad \det \mathcal{M}_s = \det (|\not{D}(0) + m_s|^2)^{1/2} > 0, \quad (2.3)$$

which follows from the hermiticity relations

$$\eta_5 \tau_1 \mathcal{M}_{ud} \tau_1 \eta_5 = \mathcal{M}_{ud}^\dagger, \quad \eta_5 \mathcal{M}_s \eta_5 = \mathcal{M}_s^\dagger, \quad (2.4)$$

that are satisfied due to chirality $\{\not{D}, \eta_5\} = 0$ and the relation $\not{D}^\dagger(\mu_I) = -\not{D}(-\mu_I)$. In the simulation algorithm the representations with the squared operators $|\not{D} + m|^2$ are used (for the strange quark, an even-odd block diagonalization enables us to get rid of the square root in Eq. (2.3)).

It is instructive to discuss the flavor symmetries of \mathcal{M}_{ud} . Besides the anomalous and baryonic U(1) symmetries, at $\mu_I = \lambda = m_{ud} = 0$ it possesses an $SU_L(2) \times SU_R(2)$ chiral symmetry. This is broken down to $SU_V(2)$ by the light quark mass and, subsequently, to $U_{\tau_3}(1)$ by the chemical potential. The subscript in the latter case indicates that the generator of the remaining symmetry is τ_3 . This U(1) symmetry is spontaneously broken by any of the expectation values $\langle \bar{\psi} \eta_5 \tau_1 \psi \rangle$, $\langle \bar{\psi} \eta_5 \tau_2 \psi \rangle$, signaling pion condensation. The spontaneous breaking of this continuous symmetry implies the presence of a Goldstone mode that leads to infrared problems for the numerical algorithm. Our implementation in (2.2) corresponds to an explicit breaking that selects the τ_2 direction for the breaking and makes the would-be massless mode a pseudo-Goldstone boson. This small explicit breaking enables us to observe spontaneous symmetry breaking by looking at the expectation value $\langle \bar{\psi} \gamma_5 \tau_2 \psi \rangle$ and, at the same time, alleviates the infrared problem mentioned above. While the simulations are performed at $\lambda > 0$, at the end of the analysis we need to take the physical limit $\lambda \rightarrow 0$ by means of an extrapolation.

The observables we consider are, besides the already mentioned pion condensate, the light quark condensate and the isospin density,

$$\langle \pi \rangle = \frac{T}{V} \frac{\partial \log \mathcal{Z}}{\partial \lambda}, \quad \langle \bar{\psi} \psi \rangle = \frac{T}{V} \frac{\partial \log \mathcal{Z}}{\partial m_{ud}}, \quad \langle n_I \rangle = \frac{T}{V} \frac{\partial \log \mathcal{Z}}{\partial \mu_I}. \quad (2.5)$$

Using Eq. (2.1) and the relations in Eq. (2.3), we specifically have

$$\begin{aligned} \langle \pi \rangle &= \frac{T}{2V} \left\langle \text{tr} \frac{\lambda}{|\not{D}(\mu_I) + m_{ud}|^2 + \lambda^2} \right\rangle, \\ \langle \bar{\psi} \psi \rangle &= \frac{T}{2V} \left\langle \text{Re tr} \frac{\not{D}(\mu_I) + m_{ud}}{|\not{D}(\mu_I) + m_{ud}|^2 + \lambda^2} \right\rangle, \\ \langle n_I \rangle &= \frac{T}{2V} \left\langle \text{Re tr} \frac{(\not{D}(\mu_I) + m_{ud})^\dagger \not{D}(\mu_I)'}{|\not{D}(\mu_I) + m_{ud}|^2 + \lambda^2} \right\rangle, \end{aligned} \quad (2.6)$$

where the prime denotes the differentiation of the operator with respect to μ_I . While the isospin density is free of ultraviolet divergences, the two condensates are subject to renormalization. For $\langle \bar{\psi} \psi \rangle$, additive divergences appear for nonzero mass, whereas the analogous situation occurs for $\langle \pi \rangle$ for $\lambda > 0$. On the one hand – since we are working at fixed physical quark mass – additive renormalization is necessary for $\bar{\psi} \psi$, which can be achieved by subtracting its value at $T = \mu_I = 0$. On the other hand, in the $\lambda \rightarrow 0$ limit no such procedure is required for the pion condensate.

In addition, multiplicative divergences also appear in both condensates, which can be canceled by the corresponding multiplicative renormalization factors Z_π and $Z_{\bar{\psi} \psi}$. From the definitions (2.5) it is clear that $Z_\pi = Z_\lambda^{-1}$ and $Z_{\bar{\psi} \psi} = Z_{m_{ud}}^{-1}$. At first sight it may appear that the two renormalization constants are independent, but in fact they coincide in renormalization schemes independent of μ_I . To see this, notice that at $\mu_I = 0$ the mass and λ are related by an isospin rotation and are thus equivalent – consequently, $Z_{m_{ud}} = Z_\lambda$ holds. Furthermore, neither of these renormalization constants are affected by the chemical potential, thus the equality holds for arbitrary μ_I . Instead of calculating $Z_{m_{ud}}$, we multiply the condensates by m_{ud} to obtain a combination in which the renormalization constants cancel. Altogether, the renormalized observables read

$$\Sigma_{\bar{\psi} \psi} = \frac{m_{ud}}{m_\pi^2 f_\pi^2} \left[\langle \bar{\psi} \psi \rangle_{T, \mu_I} - \langle \bar{\psi} \psi \rangle_{0,0} \right] + 1, \quad \Sigma_\pi = \frac{m_{ud}}{m_\pi^2 f_\pi^2} \langle \pi \rangle, \quad (2.7)$$

where we also included a normalization factor involving the pion mass $m_\pi = 135$ MeV and the chiral limit of the pion decay constant $f_\pi = 86$ MeV for convenience. In this normalization, zero-temperature leading-order chiral perturbation theory [3] predicts a gradual rotation of the condensates so that $\Sigma_{\bar{\psi}\psi}^2 + \Sigma_\pi^2 = 1$ holds irrespective of μ_I .

3. Extrapolation in the pionic source

The most crucial step in the analysis is the extrapolation $\lambda \rightarrow 0$. As we will see below, this is rather cumbersome, since the dependence on λ around zero is pronounced for most of our observables. (The physical reason behind such a strong dependence on λ will be given in Sec. 3.2 below.) For low values of T , μ_I and λ , one can use chiral perturbation theory [12] to guide the extrapolation, as was done in Ref. [10]. For temperatures close to $T_c(0)$, however, chiral perturbation theory is no longer valid. In the direct vicinity of the phase boundary to the pion condensation phase one expects the observables to be governed by the critical exponents of the universality class, in this case supposedly $O(2)$ [3], due to symmetry, associated with the transition. Away from criticality, however, this is no longer true, so that other methods are needed for the extrapolation.

Note that in the $\lambda \rightarrow 0$ limit the $U_{\tau_3}(1)$ flavor symmetry of the action (discussed in Sec. 2) becomes exact and, accordingly, the Goldstone mode associated with its spontaneous breaking exactly massless. Strictly speaking, this implies that the thermodynamic limit $V \rightarrow \infty$ should be performed prior to the $\lambda \rightarrow 0$ extrapolation. We address this subtle issue below in Sec. 4 by comparing our results on three different spatial volumes.

3.1 Naive extrapolations

To perform the λ -extrapolation of the observables in a model-independent way, we develop a spline extrapolation scheme that provides a conservative systematic error on the $\lambda \rightarrow 0$ value. The method involves a fit of the data to a spline function defined in terms of a set of nodepoints, complemented by a Monte-Carlo simulation of the nodepoints based on an action weighing the fits according to the Akaike information criterion [13]. The method is described in detail in App. A.

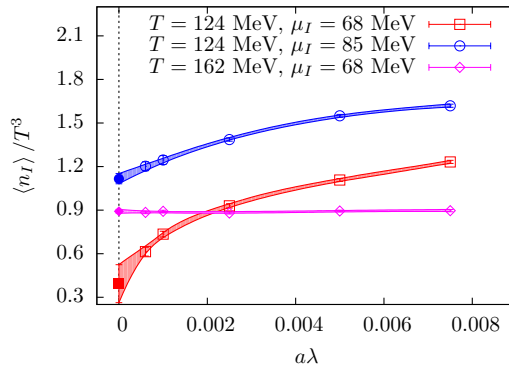


Figure 1: Results for the extrapolation of n_I using the spline Monte-Carlo outlined in the appendix.

In Fig. 1 we show typical examples of this extrapolation scheme. The isospin density is plotted for three different parameter values on $24^3 \times 6$ lattices with different λ -dependences. The plot

shows that the extrapolated values as well as the associated uncertainties indeed give a reasonable and conservative representation of the available data. In particular, for a flat dataset the spline extrapolation is similarly flat with a reasonably small uncertainty, which, in contrast to a simple linear extrapolation, also takes a possible slight curvature into account. When the extrapolation is steeper, the uncertainty of the extrapolated result increases accordingly, signaling the enhanced impact of the last few points and the associated loss in information on the extrapolated value.

3.2 Valence quark improvement

The above method works well for the extrapolation and can be applied successfully to all observables. Nevertheless, the accumulation of large uncertainties for observables where the λ -extrapolation is particularly steep is still a source for concern and a strong constraint on the accuracy concerning the investigation of the phase diagram. This is particularly true for the phase boundary to the pion condensation phase, which is defined by the onset of a non-vanishing value of the pion condensate $\langle\pi\rangle$, an example is shown in the left panel of Fig. 2. To overcome this problem, we introduce a novel approach, which uses the singular value representation of the observables of Eq. (2.6). While the basic idea can be applied to all of these observables its application to the pion condensate takes a particularly instructive form, which we will now discuss.

We begin with the singular value equation of the massive Dirac operator,

$$|\not{D}(\mu_I) + m_{ud}|^2 \psi_n = \xi_n^2 \psi_n, \quad (3.1)$$

which involves the massive singular values $\xi_n > 0$. In the basis spanned by ψ_n we can rewrite the pion condensate of Eq. (2.6) as

$$\langle\pi\rangle = \frac{\lambda T}{2V} \left\langle \sum_n (\xi_n^2 + \lambda^2)^{-1} \right\rangle \xrightarrow{V \rightarrow \infty} \frac{\lambda}{2} \left\langle \int d\xi \rho(\xi) (\xi^2 + \lambda^2)^{-1} \right\rangle \xrightarrow{\lambda \rightarrow 0} \frac{\pi}{4} \langle\rho(0)\rangle. \quad (3.2)$$

Here in the second step we considered the volume to be large enough so that the singular values become sufficiently dense and the sum can be replaced by an integral introducing the density $\rho(\xi)$ of the singular values (which includes the normalization factor T/V). In the third step we performed the $\lambda \rightarrow 0$ limit, which leads to a representation of the δ -function and results in the density $\rho(0)$ around zero. This Banks-Casher-type relation was first found in Ref. [14] for the massless case $m_{ud} = 0$. Here we have generalized it to the massive case so that the singular values depend explicitly on m_{ud} . Eq. (3.2) reveals that a nonzero pion condensate is equivalent to an accumulation of the near-zero (massive) singular values of the Dirac operator. This also explains the strong dependence of $\langle\pi\rangle$ on λ – the pionic source shifts the singular value spectrum up by an amount λ and thus impacts on the infrared physics drastically.

To be more quantitative, in the right panel of Fig. 2 we plot the integrated spectral density $N(\xi) = \int_0^\xi d\xi' \rho(\xi')$ divided by ξ , as measured on our $24^3 \times 6$ ensembles with $\lambda = 0.001$, for three different isospin chemical potentials below, close to and above the onset value $\mu_I = m_\pi/2$. Note that the $\xi \rightarrow 0$ limit of this quantity gives $\rho(0)$. The figure clearly shows that the density at zero vanishes in the normal phase but develops a nonzero expectation value in the pion condensed phase. The results for $\langle\pi\rangle$ obtained via $\langle\rho(0)\rangle$ on each $\lambda > 0$ ensemble are also shown in the left panel of Fig. 2. The plot indicates that this definition of π leads to a drastic improvement

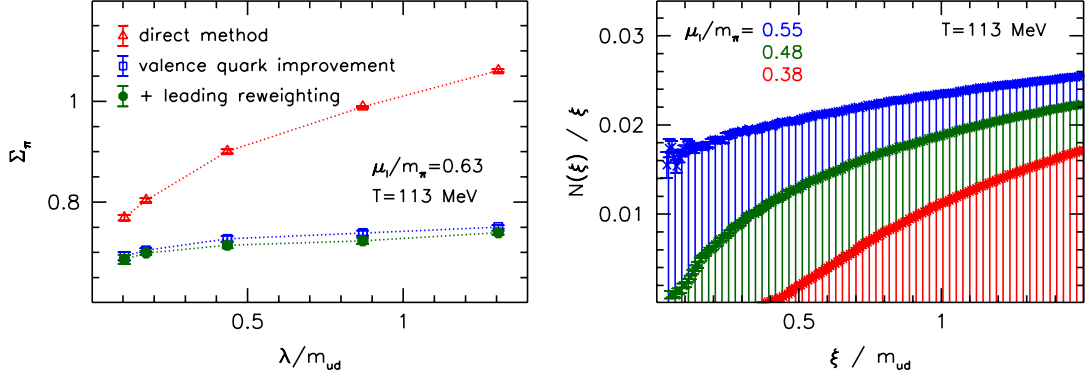


Figure 2: **Left:** Comparison of the λ -dependence of the different improved observables for the extrapolation of the pion condensate π . **Right:** Integrated spectral density of the massive singular values of the Dirac operator for various chemical potentials around the threshold value $m_\pi/2$ at low temperature $T = 113 \text{ MeV}$.

compared to the standard observable. Since this improved definition corresponds to an explicit $\lambda = 0$ substitution in the measured operator (in lattice language: in the valence sector), we denote this type of improvement as “valence quark improvement”. A similar improvement can be performed for the other observables in Eq. (2.6) as well – this will be discussed in a future publication.

3.3 Leading-order reweighting

The improvement of the operators \mathcal{O} described above corrects for most of the effects due to $\lambda > 0$ in our observables. The remaining λ -dependence originates from sea quarks, i.e. from the nonzero value of λ in the fermion determinant of the path integral measure. This can be taken into account via the reweighting approach,

$$\langle \mathcal{O} \rangle_{\lambda=0} = \frac{\langle \mathcal{O} W(\lambda) \rangle_{\lambda>0}}{\langle W(\lambda) \rangle_{\lambda>0}}, \quad W(\lambda) \equiv \frac{\det[|\not{D}(\mu_I) + m_{ud}|^2]^{1/4}}{\det[|\not{D}(\mu_I) + m_{ud}|^2 + \lambda^2]^{1/4}}, \quad (3.3)$$

where we used the relations in Eq. (2.3). Rewriting the logarithm $\log W(\lambda)$ of the reweighting factor we obtain

$$\log \frac{\det[|\not{D}(\mu_I) + m_{ud}|^2 + \lambda^2 - \lambda_w^2]^{1/4}}{\det[|\not{D}(\mu_I) + m_{ud}|^2 + \lambda^2]^{1/4}} \Bigg|_{\lambda_w=\lambda} = \left[-\lambda_w^2 \frac{V}{2T} \frac{\pi}{\lambda} + \mathcal{O}(\lambda_w^4) \right]_{\lambda_w=\lambda} = -\frac{\lambda V}{2T} \pi + \mathcal{O}(\lambda^4), \quad (3.4)$$

where we replaced the expression with its Taylor-expansion in λ_w^2 around $\lambda_w = 0$ and compared to the pion condensate (2.6). Thus we conclude that the reweighting of an observable, to leading order in λ , involves the exponential of the pion condensate times the four-volume. Since the pion condensate is anyway measured for $\langle \pi \rangle$, this improvement comes with no extra costs. The inclusion of the reweighting factors reduces the dependence of the pion condensate on λ further, as visible in the left panel of Fig. 2.

4. Results for the phase diagram

We will now discuss the results concerning the phase diagram. The focus of the present contribution is on lattices with a temporal extent $N_t = 6$, but in the next section we will also include results from $N_t = 8, 10$ and 12 lattices. We have found that the introduction of the pionic source is necessary for the stability of the simulations throughout the phase diagram – even when we are not within the phase where pions condense. The extrapolation of the results to $\lambda = 0$ is performed using the methods discussed above.

4.1 Phase boundary to the pion condensation phase

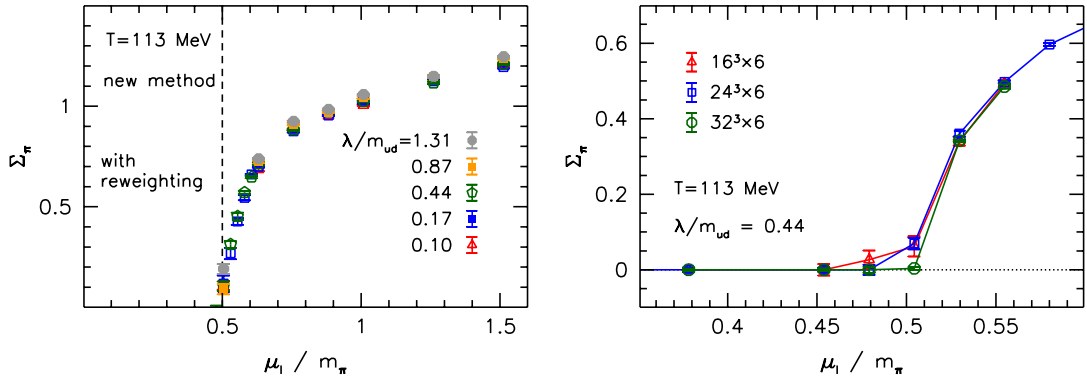


Figure 3: **Left:** Results for the improved and renormalized pion condensate on the $24^3 \times 6$ lattice at $T = 113$ MeV versus μ_I . The vertical line indicates the boundary to the pion condensation phase at $T = 0$, $\mu_I/m_\pi = 0.5$. **Right:** The volume-dependence of the same observable at fixed temperature and pionic source.

The phase boundary to the pion condensation phase is defined by the point where the system develops a non-zero pion condensate. We show the typical behavior of the improved and renormalized pion condensate, including also the leading order reweighting factor, for different values of λ in the left panel of Fig. 3. As can be seen from the plot, the phase boundary is clearly visible even for finite values of λ and the results from different λ -values, owing to the use of the improved operator, fall on top of each other. In the right panel of the figure we show the volume-dependence of Σ_π using three different spatial lattice sizes. This reveals the typical sharpening around the critical chemical potential, suggesting that a real phase transition takes place in the $V \rightarrow \infty$ limit.

In Fig. 4 we show the associated results for the phase boundary in the (T, μ_I) parameter plane for $N_t = 6, 8, 10$ and 12 . The plot indicates that the boundary of the pion condensation phase basically follows the vertical $\mu_I/m_\pi = 0.5$ line up to a temperature of about $T \approx 130$ MeV, independent of the value of N_t . More surprising is the strong flattening of the phase boundary at $T \approx 160$ MeV, which is in qualitative agreement with the findings from [5–8], but in contrast to the expectations from chiral perturbation theory [3]. Above $T \approx 130$ MeV the phase boundary also becomes more sensible to lattice artefacts, indicated by the larger spread of the points from different N_t values.

4.2 Crossover line at small density

Next, we investigate the behavior of the crossover line in the (T, μ_I) -plane, starting from the

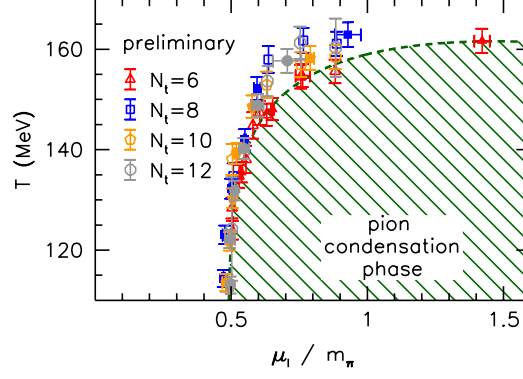


Figure 4: Results for the boundary of the pion condensation phase in the (T, μ_I) parameter plane. Open symbols are obtained from scans in the temperature, filled symbols from scans in μ_I . Besides statistical errors, the latter are also subject to an intrinsic uncertainty for T originating from the lattice scale.

well-known crossover at the physical point at $\mu_I = 0$. The main observable associated with the crossover, i.e., with the restoration of chiral symmetry, is the renormalized chiral condensate of (Eq. 2.7). The pseudocritical temperature of the crossover can be defined, for instance, by the inflection point of the condensate, see, e.g., Ref. [15]. Using this definition and the same action as in our study (for $\mu_I = 0$), the crossover temperature in the continuum limit was determined to be $T_c(0) = 155(3)(3)$ [15]. Here we will use a slightly different definition and define the crossover temperature to be the temperature where the renormalized chiral condensate acquires its continuum value at $T_c(0)$. Following Ref. [15] the value is given by $\Sigma_{\bar{\psi}\psi}|_{T_c} \approx -0.550$ in our normalization. This definition for $T_c(\mu_I)$ is adequate as long as we are in the Silver Blaze region (where the $T \rightarrow 0$ limit of the condensate is independent of μ_I) and should be compared to the results from other definitions eventually.

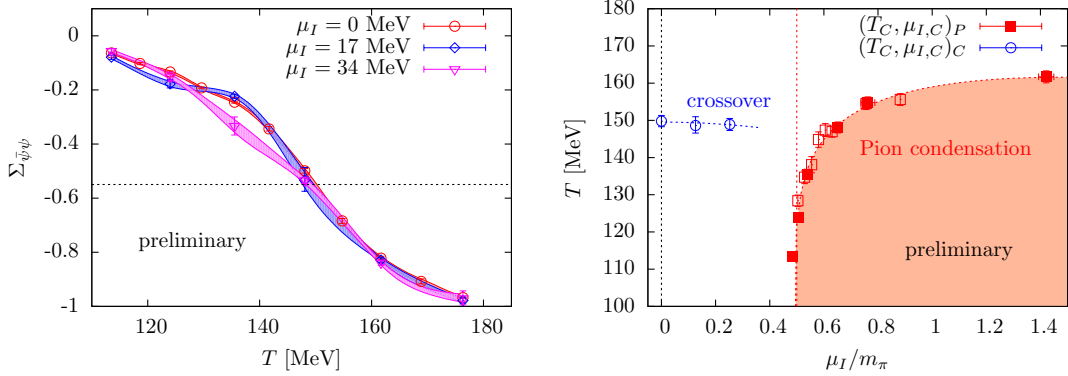


Figure 5: **Left:** Results for $\Sigma_{\bar{\psi}\psi}$ vs. the temperature for different values of μ_I . The colored areas are the results from a cubic spline interpolation and the dashed horizontal line indicates $\Sigma_{\bar{\psi}\psi}|_{T_c}$ (see text). **Right:** Phase diagram for the $24^3 \times 6$ lattice. The red points are the results for the phase boundary to the pion condensation phase, $(T_c, \mu_{I,c})_P$, and the blue points the ones for the crossover line, $(T_c, \mu_{I,c})_C$.

In the left panel of Fig. 5 we show the results for the renormalized chiral condensate versus

the temperature for different values of μ_I . The horizontal line indicates the value $\Sigma_{\bar{\psi}\psi}|_{T_c}$ and the colored bands result from cubic spline interpolations of the data points. For $\mu_I = 0$ the result for $T_c(0) = 150(3)(3)$ (where the second uncertainty is due to scale setting) is slightly smaller than the continuum result. This can be attributed to lattice artifacts which can still be sizable at $N_t = 6$. The plot shows that the result for T_c does not change significantly up to $\mu_I = 34$ MeV.

In the right panel of Fig. 5 we show the resulting phase diagram for the $24^3 \times 6$ lattice. At the physical pion mass, the crossover temperature at $\mu_I = 0$ appears to lie somewhat below the temperature associated with the melting of the pion condensate (i.e. the upper boundary of the pion condensation phase). However, notice that the chiral restoration transition is a broad crossover, whereas pion condensation sets in via a real phase transition. The nature of the latter transition will be the subject of a forthcoming publication. Hints for a critical endpoint, where the transition turns first order, were obtained on small lattices and heavier-than-physical quark masses in Refs. [6, 7].

A slight downwards trend in $T_c(\mu_I)$ is observed as the chemical potential increases. The dashed curve corresponds to a quadratic fit to the crossover temperatures. Translating the included coefficient κ into the normalization from [16] and using that, in the present setup, $3\mu_I$ compares to μ_B , we obtain $\kappa \approx 0.015$, which is of the same order of magnitude as the analogous results for nonzero baryon chemical potentials, from [17].

5. A test for Taylor expansion

One of the long-standing challenges in lattice QCD is the complex action problem, mentioned in the introduction, which hinders direct simulations at non-zero baryon chemical potential μ_B . A standard technique to circumvent this problem is the Taylor expansion method, which involves working with derivatives with respect to μ_B evaluated at $\mu_B = 0$. One of the major drawbacks of this approach is the *a priori* unknown range of applicability when working at a fixed order of the expansion. Since the Taylor expansion can be defined with respect to any of the chemical potentials in Eq. (1.1), our results at finite isospin chemical potential provide an ideal testbed for the method.

For the comparison of our direct results to the Taylor method we will focus on the isospin density n_I from Eq. (2.5). Its expansion in terms of μ_I can be written in the form

$$\frac{\langle n_I \rangle}{T^3} = c_2 \left(\frac{\mu_I}{T} \right) + \frac{c_4}{6} \left(\frac{\mu_I}{T} \right)^3. \quad (5.1)$$

Here c_2 and c_4 are Taylor coefficients, which, using the expression for the QCD pressure

$$\frac{p}{T^4} = \frac{1}{VT^3} \log \mathcal{Z}, \quad (5.2)$$

can be written as

$$c_2 = 2 \left[\partial_u^2 \left(\frac{p}{T^4} \right) - \partial_u \partial_d \left(\frac{p}{T^4} \right) \right] \quad \text{and} \quad c_4 = 2 \left[\partial_u^4 \left(\frac{p}{T^4} \right) - 4 \partial_u^3 \partial_d \left(\frac{p}{T^4} \right) + 3 \partial_u^2 \partial_d^2 \left(\frac{p}{T^4} \right) \right], \quad (5.3)$$

where ∂_f is the derivative with respect to the chemical potential to temperature ratio μ_f/T . We compare to the Taylor expansion coefficients determined in Ref. [18], which uses the same action as we do in the present study. To arrive at the coefficients corresponding to the temperatures of our simulations we have performed a cubic spline interpolation of c_2 and of c_4 .

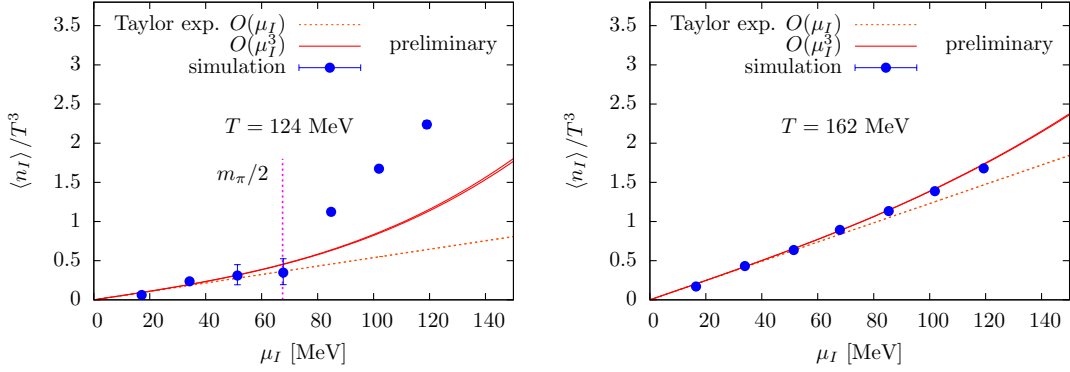


Figure 6: Comparison of the results for the isospin density from $24^3 \times 6$ lattices for temperatures 124 (left) and 162 MeV (right) and the results from Taylor expansion around $\mu_I = 0$ to $\mathcal{O}(\mu_I)$ and $\mathcal{O}(\mu_I^3)$. The dashed vertical line in the left panel indicates the phase boundary to the pion condensation phase.

The comparison for the $N_t = 6$ lattices is shown in Fig. 6 for two temperatures of 124 (left) and 162 MeV (right).¹ Based on the last section, the former temperature is below $T_c(0)$ and below the temperature associated with the melting of the pion condensate, so that we enter the pion condensation phase at $\mu_I/m_\pi \approx 0.5$, indicated by the vertical line in Fig. 6 (left). The latter temperature is above $T_c(0)$ and above the phase boundary of the pion condensation phase (at least for the values of μ_I considered here), so that we remain in the normal phase.

For $T = 124$ MeV the data agrees very well with the Taylor expansion up to the point where we enter the pion condensation phase. At this point the ground state of the system changes drastically, so that, naturally, one expects the Taylor expansion method to break down. This is indeed visible in the plot: up to this value of μ_I the Taylor expansion curves to $\mathcal{O}(\mu_I)$ and $\mathcal{O}(\mu_I^3)$ are still too close to be distinguished with the present accuracy of the data. For $T = 162$ MeV the agreement between the data and the Taylor expansion to $\mathcal{O}(\mu_I^3)$ persists for all values of μ_I considered at present (perhaps with the exception of the last point). Starting from $\mu_I/m_\pi \approx 0.5$ the term of order $\mathcal{O}(\mu_I^3)$ becomes important, so that the Taylor expansions to $\mathcal{O}(\mu_I)$ and $\mathcal{O}(\mu_I^3)$ can be distinguished. It would be interesting to generate data at larger values of μ_I to see how long the agreement between the data and the expansion to $\mathcal{O}(\mu_I^3)$ remains and we will investigate this in a future publication.

6. Conclusions

In this contribution we have presented first results from our investigation of the phase diagram of QCD in the presence of a finite isospin chemical potential, using physical quark masses and an improved staggered action. We have introduced, for the first time in this context, the massive singular value representation of the partition function and of the relevant observables. This representation lead us to a Banks-Casher-type relation that connects the pion condensate to the singular value density at zero. Employing this relation was found to drastically improve the extrapolation

¹We mention that our $N_s = 24$ ensembles are compared here to the $N_s = 18$ results of Ref. [18]. Nevertheless, we have explicitly checked by comparing results for the coefficients obtained on different volumes [18], that finite size effects on the c_i are negligible.

$\lambda \rightarrow 0$ in the pionic source – this auxiliary parameter $\lambda > 0$ is necessary in the simulations to have the infrared behavior of the system under control. Besides this valence improvement, we included reweighting factors to take into account the leading-order effect of the pionic source for the sea quarks as well. Finally, we worked out a spline Monte-Carlo scheme for performing additional extrapolations in λ in a model-independent manner.

At high values of μ_I the system was found to be in the pion condensed phase, separated from the normal phase – as our preliminary finite-volume analysis suggests – by a real phase transition. We have mapped out this phase boundary and found it, on the one hand, to be almost T -independent for temperatures below the $\mu_I = 0$ chiral crossover temperature $T_c(0) \approx 155$ MeV. On the other hand, for higher temperatures the phase boundary appears to flatten out so that no pion condensate forms above ~ 160 MeV, at least for the chemical potentials that we investigated here. A simplistic interpretation of these findings is that in the chirally restored/deconfined phase pions do not exist anymore, thus the formation of a pion condensate becomes strongly suppressed in this region.

For low chemical potentials, we calculated the dependence of the chiral/deconfinement crossover temperature on μ_I and made a rough estimate on the curvature of the transition line. In addition, we performed a quantitative comparison of our direct results to the leading- and the next-to-leading-order Taylor expansion in the isospin chemical potential at $\mu_I = 0$. Currently all results for the isospin density show good agreement with the Taylor expansion to $\mathcal{O}(\mu_I^3)$, as long as the boundary of the pion condensation phase is not crossed. The contributions from $\mathcal{O}(\mu_I^3)$ start to become important at $\mu_I/T \approx 0.5$ for $T = 162$ MeV so that the expansions to $\mathcal{O}(\mu_I)$ and $\mathcal{O}(\mu_I^3)$ can be distinguished. It will be interesting to simulate at larger values of μ_I to check where terms of $\mathcal{O}(\mu_I^5)$ become non-negligible.

To extend the present study, we plan to apply the novel techniques developed here to map out the complete phase diagram concentrating, in particular, on the meeting point of the two different transition lines and on the high- μ_I region.

Acknowledgments This research was funded by the DFG (Emmy Noether Programme EN 1064/2-1 and SFB/TRR 55). The majority of the simulations was performed on the GPU cluster of the Institute for theoretical Physics at the University of Regensburg. B. B. acknowledges support from the Frankfurter Förderverein für Physikalische Grundlagenforschung. The authors thank Szabolcs Borsányi for useful correspondence and for providing the data for the Taylor expansion coefficients.

A. A model independent spline extrapolation

A model-independent extrapolation should take into account all smooth functions that go through the available data points. A possible way to represent this function space is by means of polynomials of degree n , crafted together at a set of grid points, i.e. a spline. A particular version of spline interpolation is spline fitting (see, e.g., Ref. [19]), where the grid points are placed around and between the datapoints, so that the free parameters of the spline are determined by a fit to the data. A spline, for which the outermost grid points lie outside of the dataset constitutes an extrapolation. Typical spline fits involve the use of so-called natural boundary conditions at these outermost grid points, setting the second and higher derivatives there to zero. For the most general curve in case of an extrapolation, these higher derivatives should also be treated as free parameters.

The remaining issue with the resulting extrapolation is the dependence of the result on the number and position of the grid points. To ensure model-independence, we need to average over all possible grid point configurations. However, different sets of grid points might not allow for equivalently good descriptions of the data. Taking this into account turns the average over grid points into a weighted average. There are several possible weight factors that one can use. We will write the weight factor in the form $w = \exp(-S_{\text{spl}})$, where we have introduced the ‘‘action’’ S_{spl} . Then the average over all possible spline configurations of a quantity A can be written as

$$\langle\langle A \rangle\rangle = \sum_{N_G} \int d^{N_x(N_G)}_{\vec{x}} A(\vec{x}) \exp(-S_{\text{spl}}(\vec{x}, N_G)). \quad (\text{A.1})$$

Here the sum runs over the possible number N_G of spline grid points, we have denoted the set of grid points by \vec{x} and $N_x(N_G)$ is the number of grid points that can be varied. Note that the positions of the data points can also be restricted to certain areas. In particular, in our setup we use a rectangular grid and demand that in each direction at least one measurement is included in each interval between two grid points. The weighted sum can be performed efficiently using Monte-Carlo methods [20], e.g. via a Metropolis algorithm.

A possible choice for the action is to use the Akaike information criterion [13],

$$S_{\text{AIC}} = 2N_P + \chi^2, \quad (\text{A.2})$$

where N_P is the number of parameters of the fit. An alternative choice is to use the goodness of the fit, leading to the action

$$S_{\text{GOOD}} = P(\chi^2, N_{\text{dof}}) - 1, \quad \text{where} \quad P(\chi^2, N_{\text{dof}}) = \frac{\gamma(\chi^2/2, N_{\text{dof}}/2)}{\Gamma(N_{\text{dof}}/2)} \quad (\text{A.3})$$

is the cumulative χ^2 -distribution function, N_{dof} the number of degrees of freedom and γ the lower incomplete gamma-function. We have tested these definitions and found that the results of the λ -extrapolations from the Akaike information criterion were more robust with respect to oscillatory spline solutions (see [19] for a detailed discussion), most probably due to the explicit punishment for a large number of fit parameters.

In the present setting, we perform a one-dimensional spline extrapolation in λ for each set of bare parameters (β, μ_I) . We use cubic splines and set the second derivative of the curve at the nodepoint for the highest λ to zero and leave the second derivative at $x_1 = 0$ a free parameter. For the spline Monte-Carlo we employ the action from Eq. (A.2) and use 1000 measurements, separated by 20 updates and preceded by 1000 thermalization updates. One more compromise we had to make in order to obtain stable results was to set the lowest nodepoints so that at least two datapoints lie between $x_1 = 0$ and x_2 .

To estimate the uncertainties from the spline Monte-Carlo we have performed the spline fits for each bootstrapped sample, using the action associated with the fit to the central value in the update steps. The resulting uncertainty for the extrapolated values consists of two uncertainties: (i) the statistical uncertainty, obtained from the bootstrap samples containing the average over all spline fits for this sample; (ii) the Monte-Carlo uncertainty on the central value, obtained in the standard way from the individual fits to the central value. These two types of errors have been conservatively added in quadrature.

References

- [1] A. B. Migdal, *Pion Fields in Nuclear Matter*, *Rev. Mod. Phys.* **50** (1978) 107–172.
- [2] V. Ruck, M. Gyulassy and W. Greiner, *Pion Condensation in Heavy Ion Collisions*, *Z. Phys.* **A277** (1976) 391–394.
- [3] D. T. Son and M. A. Stephanov, *QCD at finite isospin density*, *Phys. Rev. Lett.* **86** (2001) 592–595, [[hep-ph/0005225](#)].
- [4] T. D. Cohen, *Functional integrals for QCD at nonzero chemical potential and zero density*, *Phys. Rev. Lett.* **91** (2003) 222001, [[hep-ph/0307089](#)].
- [5] J. B. Kogut and D. K. Sinclair, *Quenched lattice QCD at finite isospin density and related theories*, *Phys. Rev.* **D66** (2002) 014508, [[hep-lat/0201017](#)].
- [6] J. B. Kogut and D. K. Sinclair, *Lattice QCD at finite isospin density at zero and finite temperature*, *Phys. Rev.* **D66** (2002) 034505, [[hep-lat/0202028](#)].
- [7] J. B. Kogut and D. K. Sinclair, *The Finite temperature transition for 2-flavor lattice QCD at finite isospin density*, *Phys. Rev.* **D70** (2004) 094501, [[hep-lat/0407027](#)].
- [8] P. de Forcrand, M. A. Stephanov and U. Wenger, *On the phase diagram of QCD at finite isospin density*, *PoS LAT2007* (2007) 237, [[0711.0023](#)].
- [9] W. Detmold, K. Orginos and Z. Shi, *Lattice QCD at non-zero isospin chemical potential*, *Phys. Rev.* **D86** (2012) 054507, [[1205.4224](#)].
- [10] G. Endrődi, *Magnetic structure of isospin-asymmetric QCD matter in neutron stars*, *Phys. Rev.* **D90** (2014) 094501, [[1407.1216](#)].
- [11] S. Borsányi et al., *The QCD equation of state with dynamical quarks*, *JHEP* **11** (2010) 077, [[1007.2580](#)].
- [12] K. Splittorff, D. Toublan and J. J. M. Verbaarschot, *Thermodynamics of chiral symmetry at low densities*, *Nucl. Phys.* **B639** (2002) 524–548, [[hep-ph/0204076](#)].
- [13] S. Borsányi et al., *Ab initio calculation of the neutron-proton mass difference*, *Science* **347** (2015) 1452–1455, [[1406.4088](#)].
- [14] T. Kanazawa, T. Wettig and N. Yamamoto, *Singular values of the Dirac operator in dense QCD-like theories*, *JHEP* **12** (2011) 007, [[1110.5858](#)].
- [15] WUPPERTAL-BUDAPEST collaboration, S. Borsányi, Z. Fodor, C. Hoelbling, S. D. Katz, S. Krieg, C. Ratti et al., *Is there still any T_c mystery in lattice QCD? Results with physical masses in the continuum limit III*, *JHEP* **09** (2010) 073, [[1005.3508](#)].
- [16] G. Endrődi, Z. Fodor, S. D. Katz and K. K. Szabó, *The QCD phase diagram at nonzero quark density*, *JHEP* **04** (2011) 001, [[1102.1356](#)].
- [17] R. Bellwied, S. Borsányi, Z. Fodor, S. D. Katz, A. Pásztor, C. Ratti et al., *Fluctuations and correlations in high temperature QCD*, *Phys. Rev.* **D92** (2015) 114505, [[1507.04627](#)].
- [18] S. Borsányi, Z. Fodor, S. D. Katz, S. Krieg, C. Ratti and K. Szabó, *Fluctuations of conserved charges at finite temperature from lattice QCD*, *JHEP* **01** (2012) 138, [[1112.4416](#)].
- [19] G. Endrődi, *Multidimensional spline integration of scattered data*, *Comput. Phys. Commun.* **182** (2011) 1307–1314, [[1010.2952](#)].
- [20] S. Borsányi, *private communication*, .